Received: 23 May 2023 | Revised: 3 August 2023 | Accepted: 4 August 2023

DOI: 10.1002/dug2.12062

RESEARCH ARTICLE

DUSE WILEY

Flow field analysis and particle erosion of tunnel-slope systems under coupling between runoff and fast (slow) seepage

Shuai Zhang[1] | **Danqing Song**[2] | **Ruiliang Zhang**[3] | **Kai Zhang**[4] | **Qi Zhao**[5] | **Suraksha Sharma**[6]

[1]Department of Hydraulic Engineering, State Key Laboratory of Hydroscience and Engineering, Key Laboratory of Hydrosphere Sciences of the Ministry of Water Resources, Tsinghua University, Beijing, China

[2]School of Civil Engineering and Transportation, State Key Laboratory of Subtropical Building Science, South China University of Technology, Guangzhou, Guangdong, China

[3]Department of Geotechnical Engineering, State Key Laboratory of Hydraulic and Mountain River Engineering, Sichuan University, Chengdu, China

[4]Faculty of Civil Engineering and Mechanics, Kunming University of Science and Technology, Kunming, Yunnan, China

[5]Department of Civil and Environmental Engineering, The Hong Kong Polytechnic University, Hong Kong, China

[6]Norwegian University of Science and Technology, Trondheim, Norway

Correspondence

Danqing Song, School of Civil Engineering and Transportation, State Key Laboratory of Subtropical Bldg Science, South China University of Technology, Guangzhou, Guangdong 510640, China.
Email: dqsong@scut.edu.cn

Funding information

National Natural Science Foundation of China, Grant/Award Number: 52109125; Fundamental Research Funds for the Central Universities, Grant/Award Number: 2023ZYGXZRx2tjD2231010; Natural Science Foundation of Jiangsu Province, Grant/Award Number: BK20231217

Abstract

The presence of particles on the surface of a tunnel slope renders it susceptible to erosion by water flow, which is a major cause of soil and water loss. In this study, a nonlinear mathematical model and a mechanical equilibrium model are developed to investigate the distribution of flow fields and particle motion characteristics of tunnel slopes, respectively. The mathematical model of flow fields comprises three parts: a runoff region, a highly permeable soil layer, and a weakly permeable soil layer. The Navier–Stokes equation controls fluid motion in the runoff region, while the Brinkman-extended Darcy equation governs fast and slow seepage in the highly and weakly permeable soil layers, respectively. Analytical solutions are derived for the velocity profile and shear stress expression of the model flow field under the boundary condition of continuous transition of velocity and stress at the fluid–solid interface. The shear stress distribution shows that the shear stress at the tunnel-slope surface is the largest, followed by the shear stress of the soil interface, indicating that particles in these two locations are most vulnerable to erosion. A mechanical equilibrium model of sliding and rolling of single particles is established at the fluid–solid interface, and the safety factor of particle motion (sliding and rolling) is derived. Sensitivity analysis shows that by increasing the runoff depth, slope angle, and soil permeability, the erosion of soil particles will be aggravated on the tunnel-slope surface, but by increasing the particle diameter, particle-specific gravity, and particle stacking angle, the erosion resistance ability of the tunnel-slope surface particles will be enhanced. This study can serve as a reference for the analysis of surface soil and water loss in tunnel-slope systems.

KEYWORDS

particle erosion, particle motion, runoff-fast (slow) seepage coupling, shear stress profile, tunnel-slope system, velocity profile

Highlights

- Nonlinear models were used to study the flow field distribution and particle motion on slopes.
- The model includes three regions: runoff, highly permeable soil, and weakly permeable soil.
- Sensitivity analysis indicates that erosion is affected by runoff depth, slope angle, soil permeability, particle diameter, specific gravity, and stacking angle.

1 | INTRODUCTION

In recent years, soil and water loss has become a growing problem (Liu et al., 2021; Tsai et al., 2022), with tunnel-slope erosion being a direct cause of this phenomenon (Ciampalini & Torri, 1998; Dunkerley, 2015; Lin et al., 2022; Shen et al., 2019). Tunnel-slope erosion is highly likely, random, and dangerous, which adversely affects environmental protection (Akgun & Turk, 2011), hinders traffic development (Guo et al., 2010), and threatens people's life and property. A large number of engineering cases have shown that tunnel-slope systems are prone to particle erosion under the action of water flow in the initial stage, followed by instability and failure in the later stage (Chen et al., 2022; Jiao et al., 2022; Wei et al., 2023). Therefore, it is imperative to develop a model to evaluate particle erosion in tunnel slopes.

Richard's equation is commonly used to describe the unsaturated seepage in the initial period of rainfall on tunnel-slope surfaces, while runoff gradually forms on the slope surface with the increase of the rainfall intensity. The probability of slope erosion increases as the runoff depth increases (Arnau-Rosalén et al., 2008). Although the scouring of riverbeds has been studied extensively (Piqué et al., 2016; Xiong et al., 2017; Zhao et al., 2019), scouring problems of highway slopes, tunnel slopes, and reservoir banks continue to emerge with the continuous development of transportation and water conservancy (Chehlafi et al., 2019; Liu et al., 2010; Wang et al., 2020).

Compared with clay tunnel slopes, sandy slopes have almost negligible particle cohesion, thus being more prone to soil erosion (Liu et al., 2019). The effects of tunnel-slope gradients on scouring rate have been studied by Fox and Bryan (2000), who found that the runoff velocity and soil loss are positively correlated with the tunnel-slope gradient during rainfall scour tests. Berger et al. (2010) conducted rainfall simulation indoor scouring experiments on slopes with varying slope gradients and rainfall intensities, discovering that the change in rainfall intensity has a more significant impact on sediment yield than the slope gradient. Mendes et al. (2007) noted that the critical erosion shear stress, which is affected by slope gradient, hydrostatic pressure, and water density, can determine whether particles will move or not. Patricia et al. (1987) studied the particle motion of homogeneous/heterogeneous particles and derived an analytical solution of the critical shear stress for noncohesive sediment based on the force balance of a single particle. Xie et al. (2009) proposed a formula for the critical shield number used to evaluate the incipient motion of cohesionless particles, which increases with the slope angle and hydraulic gradient of seepage. When water acts on tunnel-slope particles, additional forces, such as drag force, lift force, and buoyancy force, come into play, leading to particle instability (He & Tafti, 2018; Sugioka & Komori, 2007; Zastawny et al., 2012). Seepage force can also promote particle initiation and intensify slope erosion, particularly when the slope has high permeability (Liu & Chiew, 2012; Yergey et al., 2010). Theoretical models for judging particle initiation are primarily derived from mechanical equilibrium (Guo et al., 2019; Zhai et al., 2020). The critical shear stress, critical velocity, critical water depth, and particle start-up safety factor are commonly used parameters to identify particle scouring, while the influence of vegetation on slope particle erosion has also been studied (Cheng et al., 2020; Kim et al., 2015, 2018).

Currently, the tunnel slope is regarded as a homogeneous soil layer in studies on flow field characteristics and scouring erosion (Agudo & Wierschem, 2012; Rabinovich & Kalman, 2009), with no reports on double-layer rock and soil mass slopes with different permeability characteristics. Moreover, the coupling effect of runoff and seepage is not considered in current studies on slope particle erosion (Cui et al., 2019).

In this study, a nonlinear mathematical model is proposed to investigate the effects of free runoff on the tunnel-slope surface coupled with saturated seepage in tunnel-slope bodies, including highly and weakly permeable soil layers. The runoff is governed by the Navier–Stokes equation, while the seepage is described by the Brinkman–extended Darcy equation. Analytical solutions of pressure, velocity, and shear stress are derived for cases where the interface velocity and shear stress remain continuous. Based on a single-particle mechanical equilibrium model, in this study, the effects of various slopes, runoff depths, and permeability on velocity and shear stress, as well as the particle motion of the tunnel-slope surface are analyzed. The expressions of the particle motion safety factor are derived based on a sliding model and a rolling model, and the parameter sensitivity of the particle rolling safety factor is discussed.

2 | THEORETICAL ANALYSIS OF THE FLOW FIELD

Tropical and subtropical regions are home to a significant number of eluvial soil-strongly weathered rock stratum slopes (Ma et al., 2018; Zhan et al., 2013). The cross-section of the tunnel-slope system is illustrated in Figure 1a, where the surface soil of the tunnel slope is eluvial soil with high hydraulic conductivity ability. Underneath the eluvial soil layer lies a strongly weathered rock stratum, which can be regarded as a weakly permeable layer. The bottom of the strongly weathered rock stratum is an impermeable rock stratum. A locally enlarged model of the studied tunnel slope is shown in Figure 1b, which comprises three parts, that is, the runoff region, the highly permeable soil layer (eluvial soil), and the weakly permeable soil layer (strongly weathered rock stratum). The fluid in the runoff region is unconstrained free flow. However, the fluids in highly/weakly permeable soil layers show fast/slow seepage, respectively. The model length and total width are L and H, respectively; the slope angle is θ; the runoff depth is h; the velocities of runoff, fast seepage, and slow seepage along the x direction are v_{rx}, v_{sx1}, and v_{sx2}, respectively; v_{sy1} is the fast seepage velocity along the y direction; $\overline{v_i}$ is the interface velocity between runoff and fast seepage; v is the actual seepage velocity; and the widths of the highly/weakly permeable soil layers are b_1 and b_2, respectively. As the fluid motion of runoff and seepage in slopes is a complex problem, the theoretical derivations are based on the following assumptions.

1. The highly/weakly soil layers are isotropic and homogeneous porous media (Zhang & Liu, 2023).
2. The seepage flow is statured seepage (Ye et al., 2019).
3. Runoff and seepage are steady and laminar (Yuan et al., 2019).
4. The fluid is an incompressible Newtonian fluid (Wei et al., 2018).
5. The dissolution of chemicals and the formation of bubbles in the fluid are ignored.
6. The fluid motion in the z direction is ignored (Liu et al., 2023).

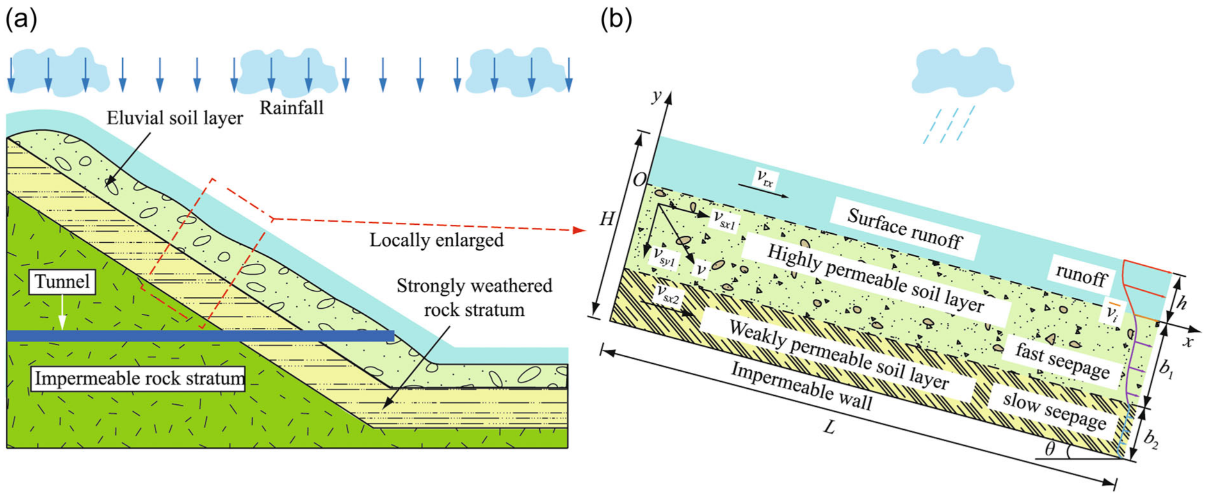

FIGURE 1 Schematic diagram of the tunnel-slope system showing runoff and seepage: (a) slope cross-section and (b) locally enlarged model.

2.1 | Governing equation

Based on the fundamental laws of fluid mechanics and soil mechanics, in this study, the parameters written in the text as governing equations to describe the physical behavior of the tunnel-slope system under the influence of water flow are derived. Specifically, the Navier–Stokes equation is used to describe the fluid flow in the runoff region, and the Brinkman-extended Darcy equation is used to describe the fast and slow seepage in the highly and weakly permeable soil layers, respectively. The analytical solutions derived from the governing equations provide insight into the velocity profile and shear stress distribution of the model flow field under different boundary conditions.

2.1.1 | Runoff flow on the slope surface

The incompressible runoff on the tunnel-slope surface obeys the continuity equation:

$$\frac{\partial v_{rx}}{\partial x} + \frac{\partial v_{ry}}{\partial y} + \frac{\partial v_{rz}}{\partial z} = 0, \tag{1}$$

where v_{rx}, v_{ry}, and v_{rz} are the actual velocities along the x, y, and z directions, respectively.

The fluid motion of the runoff is governed by the Navier–Stokes equation (Zhang, Ye, et al., 2021):

$$f_x - \frac{1}{\rho}\frac{\partial p_0}{\partial x} + \upsilon\left(\frac{\partial^2 v_{rx}}{\partial x^2} + \frac{\partial^2 v_{rx}}{\partial y^2} + \frac{\partial^2 v_{rx}}{\partial z^2}\right) = \frac{\partial v_{rx}}{\partial t} + \left(v_{rx}\frac{\partial v_{rx}}{\partial x} + v_{ry}\frac{\partial v_{rx}}{\partial y} + v_{rz}\frac{\partial v_{rx}}{\partial z}\right), \tag{2}$$

$$f_y - \frac{1}{\rho}\frac{\partial p_0}{\partial y} + \upsilon\left(\frac{\partial^2 v_{ry}}{\partial x^2} + \frac{\partial^2 v_{ry}}{\partial y^2} + \frac{\partial^2 v_{ry}}{\partial z^2}\right) = \frac{\partial v_{ry}}{\partial t} + \left(v_{rx}\frac{\partial v_{ry}}{\partial x} + v_{ry}\frac{\partial v_{ry}}{\partial y} + v_{rz}\frac{\partial v_{ry}}{\partial z}\right), \tag{3}$$

where f_x and f_y denote the mass forces of runoff along the x and y directions, respectively; ρ is the density of the fluid; t is time; p_0 is the runoff fluid pressure; and υ is the kinematic viscosity of the runoff fluid.

According to the hypothesis of runoff laminar flow, the runoff fluid only moves along the slope (x direction), that is, the runoff velocity along other directions is 0 ($v_{ry} = v_{rz} = 0$). Hence, $\partial v_{ry}/\partial y = \partial v_{rz}/\partial z = 0$. By substituting $\partial v_{ry}/\partial y = \partial v_{rz}/\partial z = 0$ into Equation (1), $\partial v_{rx}/\partial x = 0$. This implies that v_{rx} does not change in the x direction, that is, $\partial^2 v_{rx}/\partial x^2 = 0$. As the fluid motion in the z direction is ignored, it can be concluded that $\partial v_{rx}/\partial z = 0$. The mass force of the fluids only contains gravity. The component of the mass force in the x direction $f_x = g\sin\theta$ and in the y direction $f_y = g\cos\theta$; g is gravity acceleration. The velocity of fluid motion does not change with time according to the steady flow assumption, so $\partial v_{rx}/\partial t = 0$. By substituting these conditions into Equation (2), the Navier–Stokes equation in the x direction can be simplified as follows:

$$\mu_f \frac{\partial^2 v_{rx}}{\partial y^2} + \frac{\partial p_0}{\partial x} + \rho g \sin\theta = 0, \tag{4}$$

where μ_f is the fluid dynamic viscosity and $\mu_f = \rho\upsilon$.

Similarly, the Navier–Stokes equation in the y direction can be simplified as follows:

$$\frac{\partial p_0}{\partial y} + \rho g \cos\theta = 0. \tag{5}$$

2.1.2 | Fast seepage flow in the highly permeable soil layer

The fast seepage in the highly permeable soil layer satisfies the continuity equation and the Brinkman-extended Darcy equation (Zhang, Zhang, et al., 2021):

$$\frac{\partial v_{sx1}}{\partial x} + \frac{\partial v_{sy1}}{\partial y} + \frac{\partial v_{sz1}}{\partial z} = 0, \tag{6}$$

$$\rho f_x - \frac{\mu_f}{K_1} v_{sx1} - \frac{\partial p_1}{\partial x} + \mu_{eff1}\left(\frac{\partial^2 v_{sx1}}{\partial x^2} + \frac{\partial^2 v_{sx1}}{\partial y^2} + \frac{\partial^2 v_{sx1}}{\partial z^2}\right) = \frac{\rho}{n_1}\left(\frac{\partial v_{sx1}}{\partial t} + v_{sx1}\frac{\partial v_{sx1}}{\partial x} + v_{sy1}\frac{\partial v_{sx1}}{\partial y} + v_{sz1}\frac{\partial v_{sx1}}{\partial z}\right), \tag{7}$$

$$\rho f_y - \frac{\mu_f}{K_1} v_{sy1} - \frac{\partial p_1}{\partial y} + \mu_{eff1}\left(\frac{\partial^2 v_{sy1}}{\partial x^2} + \frac{\partial^2 v_{sy1}}{\partial y^2} + \frac{\partial^2 v_{sy1}}{\partial z^2}\right) = \frac{\rho}{n_1}\left(\frac{\partial v_{sy1}}{\partial t} + v_{sx1}\frac{\partial v_{sy1}}{\partial x} + v_{sy1}\frac{\partial v_{sy1}}{\partial y} + v_{sz1}\frac{\partial v_{sy1}}{\partial z}\right), \tag{8}$$

where v_{sx1}, v_{sy1}, and v_{sz1} are the actual velocities of fast seepage in the highly permeable soil layer along the x, y, and z directions, respectively. K_1 is the permeability of the highly permeable soil layer. p_1 is the fluid pressure of the fast seepage; μ_{eff1} is the effective viscosity of the fast seepage; and n_1 is the porosity of the highly permeable soil layer.

As fast seepage is laminar flow moving along the slope (x direction), the fast seepage fluid motion along the other direction is 0 ($v_{sy1} = v_{sz1} = 0$), so $\partial v_{sy1}/\partial y = \partial v_{sz1}/\partial z = 0$. Substituting these conditions into Equation (6), it can be concluded that $\partial v_{sx1}/\partial x = 0$, implying that v_{sx1} does not change along the x direction., that is, $\partial^2 v_{sx1}/\partial x^2 = 0$. As the seepage flow only moves in the x and y directions, $\partial v_{sx1}/\partial z = 0$. The mass force of the seepage fluid only contains gravity. The component of the mass force in the x direction $f_x = g \sin\theta$ and in the y direction $f_y = g\cos\theta$. The fast seepage is steady seepage; therefore, $\partial v_{sx1}/\partial t = 0$. By substituting these conditions into Equation (7), the governing equation of the fast seepage along the x direction can be simplified in Equation (9):

$$\mu_{eff1}\frac{d^2 v_{sx1}}{dy^2} + \frac{\partial p_1}{\partial x} + \rho g \sin\theta - \frac{\mu_f}{K_1} v_{sx1} = 0. \tag{9}$$

Similarly, the governing equation of the fast seepage along the y direction can be simplified as follows:

$$\frac{\partial p_1}{\partial y} + \rho g \cos\theta = 0. \tag{10}$$

2.1.3 | Slow seepage flow in the weakly permeable soil layer

The slow seepage in the weakly permeable soil layer can be described by the continuity equation and the Brinkman-extended Darcy equation:

$$\frac{\partial v_{sx2}}{\partial x} + \frac{\partial v_{sy2}}{\partial y} + \frac{\partial v_{sz2}}{\partial z} = 0, \tag{11}$$

$$\rho f_x - \frac{\mu_f}{K_2} v_{sx2} - \frac{\partial p_2}{\partial x} + \mu_{eff2}\left(\frac{\partial^2 v_{sx2}}{\partial x^2} + \frac{\partial^2 v_{sx2}}{\partial y^2} + \frac{\partial^2 v_{sx2}}{\partial z^2}\right) = \frac{\rho}{n_2}\left(\frac{\partial v_{sx2}}{\partial t} + v_{sx2}\frac{\partial v_{sx2}}{\partial x} + v_{sy2}\frac{\partial v_{sx2}}{\partial y} + v_{sz2}\frac{\partial v_{sx2}}{\partial z}\right), \tag{12}$$

$$\rho f_y - \frac{\mu_f}{K_2} v_{sy2} - \frac{\partial p_2}{\partial x} + \mu_{eff2}\left(\frac{\partial^2 v_{sy2}}{\partial x^2} + \frac{\partial^2 v_{sy2}}{\partial y^2} + \frac{\partial^2 v_{sy2}}{\partial z^2}\right) = \frac{\rho}{n_2}\left(\frac{\partial v_{sy2}}{\partial t} + v_{sx2}\frac{\partial v_{sy2}}{\partial x} + v_{sy2}\frac{\partial v_{sy2}}{\partial y} + v_{sz2}\frac{\partial v_{sy2}}{\partial z}\right), \tag{13}$$

where v_{sx2}, v_{sy2}, and v_{sz2} are the actual velocities of slow seepage in the weakly permeable soil layer along the x, y, and z directions, respectively; K_2 is the permeability of the weakly permeable soil layer. p_2 is the slow seepage fluid pressure; μ_{eff2} is the effective viscosity of the slow seepage; and n_2 is the porosity of the weakly permeable soil layer.

Similarly, the governing equations of the slow seepage in the x and y directions can be simplified as follows:

$$\mu_{eff2}\frac{d^2 v_{sx2}}{dy^2} + \frac{\partial p_2}{\partial x} + \rho g \sin\theta - \frac{\mu_f}{K_2} v_{sx2} = 0, \tag{14}$$

$$\frac{\partial p_2}{\partial y} + \rho g \cos\theta = 0. \tag{15}$$

2.2 | Pressure

By integrating Equations (5), (10), and (15), the pressures of different regions for the present model can be obtained, which are as follows:

The pressure profile of the runoff region:

$$p_0 = (h - y)\rho g \cos\theta \quad (0 < y < h). \tag{16}$$

The pressure profile of the highly permeable soil layer region:

$$p_1 = (h - y)\rho g \cos\theta \quad (-b_1 < y < 0). \tag{17}$$

The pressure profile of the weakly permeable soil layer region:

$$p_2 = (h - y)\rho g \cos\theta \quad (-b_1 - b_2 < y < b_1). \tag{18}$$

In this model, it is known from Equations (16)–(18) that the pressure profile is only a function of y and not x. Thus, the derivative or rate of change of pressure p along the x direction is 0:

$$\frac{\partial p}{\partial x} = 0. \tag{19}$$

2.3 | Velocity

The following dimensionless parameters can transform the dimensional Equations (4), (9), and (14), which represent the governing equations of free runoff and saturated seepage, into their dimensionless form.

$$Y = \frac{y}{H},\ M_i = \frac{\mu_{effi}}{\mu_f},\ Da_i = \frac{K_i}{H^2},\ S_i = \frac{1}{\sqrt{M_i Da_i}},\quad V = \frac{\mu_f v}{\rho g \sin\theta H^2} \quad (i = 1, 2), \tag{20}$$

where Y is the dimensionless position; M is the viscosity ratio; Da is the Darcy number of the soil layer; S is the particle shape coefficient; V is the dimensionless velocity; and i is the ith soil number.

Furthermore, the viscosity ratio M is related to the porosity n (Almalki & Hamdan, 2016): $M_i = f_i\sqrt{f_i}/(3\sqrt{f_i} - 3\tanh\sqrt{f_i})$, where $f_i = n_i/Da_i$, Da_i and n_i are the Darcy number and porosity of the ith porous soil layer ($i = 1, 2$), respectively.

The dimensionless expressions of the fluid motion governing Equations (4), (9), and (14) are shown in Equations (21), (22), and (23):

$$\frac{\mathrm{d}^2 V_\mathrm{r}}{\mathrm{d}Y^2} + 1 = 0 \quad (Y \in [0, \gamma_0]), \tag{21}$$

$$\frac{\mathrm{d}^2 V_{\mathrm{s}1}}{\mathrm{d}Y^2} + \frac{1}{M_1} - S_1{}^2 V_{\mathrm{s}1} = 0 \quad (Y \in (\gamma_1, 0)), \tag{22}$$

$$\frac{\mathrm{d}^2 V_{\mathrm{s}2}}{\mathrm{d}Y^2} + \frac{1}{M_2} - S_2{}^2 V_{\mathrm{s}2} = 0 \quad (Y \in [\gamma_2, \gamma_1]), \tag{23}$$

where V_r is the dimensionless runoff velocity and $V_{\mathrm{s}1}$ and $V_{\mathrm{s}2}$ are the dimensionless seepage velocities in the highly and weakly permeable soil layers, respectively; γ_0, γ_1, and γ_2 are the runoff–fast seepage interface, fast–slow seepage interface, and slow seepage–impervious wall interface, respectively.

By integrating Equations (21)–(23), the analytical solutions of the dimensionless velocity profile are as follows:

$$V_{\mathrm{s}2} = \frac{1}{M_2 S_2{}^2} + X_1 \mathrm{e}^{S_2 Y} + X_2 \mathrm{e}^{-S_2 Y} \quad (Y \in [\gamma_2, \gamma_1]), \tag{24}$$

$$V_{\mathrm{s}1} = \frac{1}{M_1 S_1{}^2} + X_3 \mathrm{e}^{S_1 Y} + X_4 \mathrm{e}^{-S_1 Y} \quad (Y \in (\gamma_1, 0)), \tag{25}$$

$$V_\mathrm{r} = -\frac{1}{2} Y^2 + X_5 Y + X_6 \quad (Y \in [0, \gamma_0]), \tag{26}$$

where X_1, X_2, X_3, X_4, X_5, and X_6 are undetermined coefficients.

Substituting Equation (20) into Equations (24)–(26), the dimensional analytical solutions of the runoff-seepage velocities are as follows:

$$v_{\mathrm{s}2} = \left(\frac{1}{M_2 S_2{}^2} + X_1 \mathrm{e}^{S_2 y/H} + X_2 \mathrm{e}^{-S_2 y/H}\right)\rho g \sin\theta H^2/\mu_\mathrm{f}, \quad (y \in [-b, -b_1]), \tag{27}$$

$$v_{\mathrm{s}1} = \left(\frac{1}{M_1 S_1{}^2} + X_3 \mathrm{e}^{S_1 y/H} + X_4 \mathrm{e}^{-S_1 y/H}\right)\rho g \sin\theta H^2/\mu_\mathrm{f}, \quad (y \in (-b_1, 0)), \tag{28}$$

$$v_\mathrm{r} = \left[-\frac{1}{2}(y/H)^2 + X_5 (y/H) + X_6\right]\rho g \sin\theta H^2/\mu_\mathrm{f}, \quad (y \in [0, h]), \tag{29}$$

To obtain the expressions of the undetermined coefficients X_1–X_6, the boundary conditions of the present model for the runoff and seepage motion are as follows:

1. At the interface between the weakly permeable soil layer and the impervious bedrock wall ($Y = \gamma_2 = -(b_1 + b_2)/H$), the velocity does not slip:

$$V_{\mathrm{s}2} = 0. \tag{30}$$

2. At the interface between the weakly permeable soil layer and the highly permeable soil layer ($Y = \gamma_1 = -b_1/H$), the velocity and shear stress remain continuous:

$$V_{\mathrm{s}2} = V_{\mathrm{s}1}, \tag{31}$$

$$M_2 \frac{\mathrm{d}V_{\mathrm{s}2}}{\mathrm{d}Y} = M_1 \frac{\mathrm{d}V_{\mathrm{s}1}}{\mathrm{d}Y}. \tag{32}$$

3. At the slope surface ($Y = 0$), the velocity and shear stress also remain continuous:

$$V_{\mathrm{s}1} = V_\mathrm{r}, \tag{33}$$

$$M_1 \frac{\mathrm{d}V_{\mathrm{s}1}}{\mathrm{d}Y} - \frac{\mathrm{d}V_\mathrm{r}}{\mathrm{d}Y} = 0, \tag{34}$$

4. At the runoff free surface ($Y = \gamma_0 = h/H$), the runoff velocity reaches its maximum values:

$$\frac{\mathrm{d}V_\mathrm{r}}{\mathrm{d}Y} = 0. \tag{35}$$

Substituting dimensionless velocity expressions Equations (24)–(26) into Equations (30)–(35), the following matrix equations can be obtained:

$$\boldsymbol{AX} = \boldsymbol{B}, \tag{36}$$

where $\boldsymbol{A}$ is a 6×6 coefficient matrix; $\boldsymbol{X}$ is a column vector of undetermined coefficients with six elements; and $\boldsymbol{B}$ is a column vector with six elements.

$$\boldsymbol{A} = \begin{vmatrix} \mathrm{e}^{S_2\gamma_2} & \mathrm{e}^{-S_2\gamma_2} & 0 & 0 & 0 & 0 \\ \mathrm{e}^{S_2\gamma_1} & \mathrm{e}^{-S_2\gamma_1} & -\mathrm{e}^{S_1\gamma_1} & -\mathrm{e}^{-S_1\gamma_1} & 0 & 0 \\ M_2 S_2 \mathrm{e}^{S_2\gamma_1} & -M_2 S_2 \mathrm{e}^{-S_2\gamma_1} & -M_1 S_1 \mathrm{e}^{S_1\gamma_1} & M_1 S_1 \mathrm{e}^{-S_1\gamma_1} & 0 & 0 \\ 0 & 0 & 1 & 1 & 0 & -1 \\ 0 & 0 & M_1 S_1 & -M_1 S & -1 & 0 \\ 0 & 0 & 0 & 0 & 1 & 0 \end{vmatrix},$$
$$\boldsymbol{X} = \begin{vmatrix} X_1 \\ X_2 \\ X_3 \\ X_4 \\ X_5 \\ X_6 \end{vmatrix}, \boldsymbol{B} = \begin{vmatrix} -1/\left(M_2 S_2^2\right) \\ 1/\left(M_1 S_1^2\right) - 1/\left(M_2 S_2^2\right) \\ 0 \\ -1/\left(M_1 S_1^2\right) \\ 0 \\ \gamma_0 \end{vmatrix}. \tag{37}$$

The expressions of X_1–X_6 can be solved using the Gaussian elimination method:

$$\begin{cases} X_1 = \dfrac{-e^{-S_2\gamma_1}a_1 + e^{-S_2\gamma_2}a_2}{2M_2S_1S_2^2a_3} \\ X_2 = -\dfrac{e^{S_2\gamma_1}a_4 + e^{S_2\gamma_2}a_2}{2M_2S_1S_2^2a_3} \\ X_3 = -\dfrac{2M_1S_1^2 + a_5}{4M_1S_1^2S_2a_3} \\ X_4 = -\dfrac{2M_1S_1^2 + a_6}{4M_1S_1^2S_2a_3} \\ X_5 = -\gamma_0 \\ X_6 = -\dfrac{a_7 + a_8}{M_1S_1^2S_2a_3} \end{cases}, \tag{38}$$

where a_1–a_8 are temporary variables.

$$a_1 = S_1[M_2S_2\cosh(S_1\gamma_1) + M_1S_1\sinh(S_1\gamma_1)], \tag{39}$$

$$a_2 = M_2S_1S_2^2\gamma_0 + \left(M_1S_1^2 - M_2S_2^2\right)\sinh(S_1\gamma_1), \tag{40}$$

$$\begin{aligned} a_3 = {} & M_2S_2\cosh(S_1\gamma_1)\cosh(S_2\gamma_1 - S_2\gamma_2) \\ & - M_1S_1\sinh(S_1\gamma_1)\sinh(S_2\gamma_1 - S_2\gamma_2), \end{aligned} \tag{41}$$

$$a_4 = S_1[M_2S_2\cosh(S_1\gamma_1) - M_1S_1\sinh(S_1\gamma_1)], \tag{42}$$

$$\begin{aligned} a_5 = {} & e^{-S_1\gamma_1 - S_2\gamma_1 + S_2\gamma_2}\Big[e^{S_1\gamma_1}\left(-M_1S_1^2 + M_2S_2^2\right) \\ & + S_1S_2(M_1S_1 - M_2S_2)\gamma_0\Big] \\ & + e^{-S_1\gamma_1 + S_2\gamma_1 - S_2\gamma_2}\Big[e^{S_1\gamma_1}\left(-M_1S_1^2 + M_2S_2^2\right) \\ & - S_1S_2(M_1S_1 + M_2S_2)\gamma_0\Big], \end{aligned} \tag{43}$$

$$\begin{aligned} a_6 = {} & e^{-S_1\gamma_1 - S_2\gamma_1 + S_2\gamma_2}\Big[e^{S_1\gamma_1}\left(-M_1S_1^2 + M_2S_2^2\right) \\ & + e^{2S_1\gamma_1}S_1S_2(M_1S_1 - M_2S_2)\gamma_0\Big] \\ & + e^{S_2\gamma_1 - S_2\gamma_2}\Big[M_2S_2^2\left(1 + e^{S_1\gamma_1}S_1\gamma_0\right) \\ & - M_1S_1^2\left(1 + e^{S_1\gamma_1}S_2\gamma_0\right)\gamma_0\Big], \end{aligned} \tag{44}$$

$$\begin{aligned} a_7 = {} & \cosh(S_2\gamma_1 - S_2\gamma_2)\Big[-M_1S_1^2 + M_2S_2^2 \\ & \left(1 - \cosh(S_1\gamma_1) + S_1\gamma_0\sinh(S_1\gamma_1)\right)\Big], \end{aligned} \tag{45}$$

$$\begin{aligned} a_8 = {} & M_1S_1\Big[S_1 + S_2\Big(-S_1\gamma_0\cosh(S_1\gamma_1) \\ & + \sinh(S_1\gamma_1)\Big)\sinh(S_2\gamma_1 - S_2\gamma_2)\Big]. \end{aligned} \tag{46}$$

The porosity values of highly permeable soil layer n_1 and weakly permeable soil layer n_2 are set as 0.40 and 0.35, respectively. The permeability of highly permeable soil layer K_1 is 3.57×10^{-8} m^2 and that of weakly permeable soil layer K_2 is 4.26×10^{-10} m^2. The height of the weakly/highly permeable soil layers and the runoff depth are $b_2 = 0.5$ m, $b_1 = 0.5$ m, and $h = 0.01$ m, respectively. The slope ratio $S_r = 0.003$; the fluid density is $\rho = 1000$ kg/m^3; the gravity acceleration is $g = 9.81$ m/s^2; and the fluid dynamic viscosity is $\mu_f = 1.006 \times 10^{-3}$ kg/(m·s). The velocity profiles under various slopes, runoff depths, and permeabilities are discussed.

The velocity profile of the present model under various slopes is shown in Figure 2. The maximum velocity value appears on the runoff surface. The greater the velocity gradient, the closer the distance to the runoff surface; also, the velocity value decreases sharply as the distance approaches the soil and water interface. The velocity profile in the highly permeable soil layer is similar to that in the runoff region, while the velocity profile in the weakly permeable soil layer is linearly distributed. Generally, the model velocity increases with steeper slopes, and the velocity in the runoff region is much higher than that in the seepage region.

The runoff velocity increases as the runoff depth increases (Figure 3a). This is because the increase in runoff depth corresponds to an increase in fluid potential energy, which is transformed into kinetic energy as the runoff flows from high to low, leading to a continuous increase in runoff velocity. Additionally, the seepage flow velocity near the soil and water interface increases with an increase in runoff depth (Figure 3b), which is attributed to the viscosity of the fluid. In other words, a fast-moving fluid will drive a slow-moving fluid. However, the seepage velocity in the weakly permeable soil layer is almost unaffected by varying the runoff depth (Figure 3c).

The model velocity distribution is shown in Figure 4 when the permeability of the highly permeable soil layer is different. With the increase in highly permeable soil layer permeability, the runoff velocity and seepage velocity in the weakly permeable soil layer increase slightly, while the seepage velocity in the highly permeable soil layer increases significantly. The main reason for this is that the soil resistance to particles decreases and the seepage velocity increases when the soil permeability increases.

2.4 | Shear stress

The shear stress profile of the three regions for the present model can be obtained by Newton's law of internal friction (Equation (47)):

$$\tau = \mu_f \frac{dv}{dy}. \tag{47}$$

By substituting Equations (27)–(29) into Equation (47), the shear stress profile expressions can be shown as follows:

$$\tau_{s2} = \left(X_1e^{S_2y/H} - X_2e^{-S_2y/H}\right)\rho g\sin\theta HS_2, \quad (y \in [-b_1, -b]), \tag{48}$$

$$\tau_{s1} = \left(X_3e^{S_1y/H} - X_4e^{-S_1y/H}\right)\rho g\sin\theta HS_1, \quad (y \in (-b, 0)), \tag{49}$$

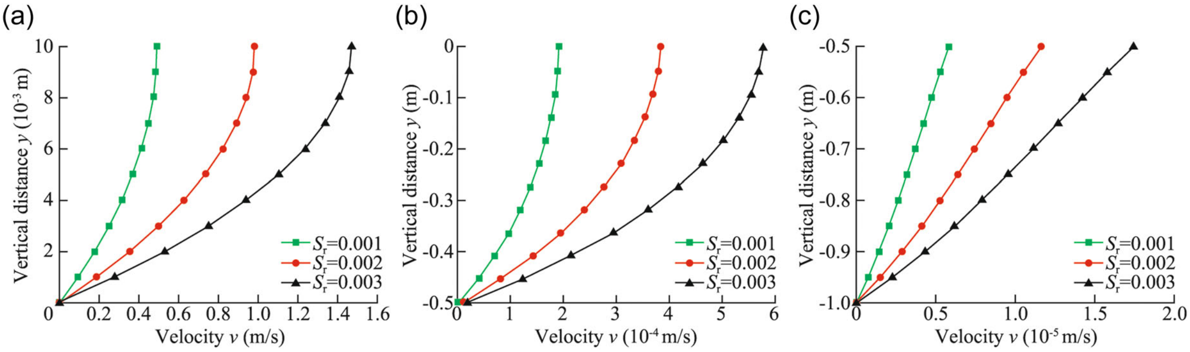

FIGURE 2 Velocity profile under various slopes: (a) runoff flow; (b) seepage flow in the highly permeable soil layer; and (c) seepage flow in the weakly permeable soil layer.

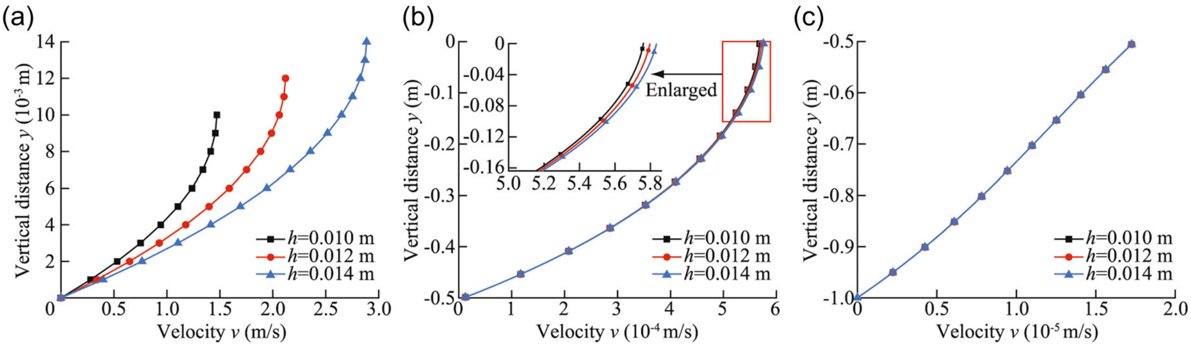

FIGURE 3 Velocity profile under various runoff depths: (a) runoff flow; (b) seepage flow in the highly permeable soil layer; and (c) seepage flow in the weakly permeable soil layer.

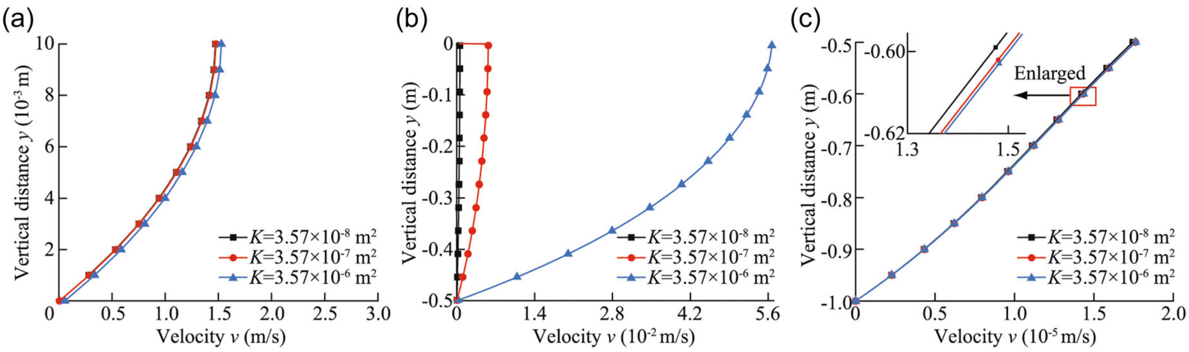

FIGURE 4 Velocity profile under various permeabilities of the highly permeable soil layer: (a) runoff flow; (b) seepage flow in the highly permeable soil layer; and (c) seepage flow in the weakly permeable soil layer.

$$\tau_r = \left(-\frac{y}{H} + X_5\right)\rho g \sin\theta H \quad (y \in [0, h]). \tag{50}$$

where τ_{s2}, τ_{s1}, and τ_r denote the shear stresses of seepage in the weakly/highly permeable soil layers and runoff at the surface, respectively.

The shear stress profile under various slopes is shown in Figure 5. The shear stress is linearly distributed in the runoff region and reaches its maximum value at the soil and water interface, indicating that this is where particle scouring often occurs. The shear stress profile undergoes a gradual linear-to-nonlinear transition from the runoff region to the highly permeable soil layer and then to the weakly permeable soil layer. In the runoff and highly permeable soil regions, the shear stress increases toward the bottom. However, in the weakly permeable soil region, the shear stress near the top and bottom interfaces is high, while the shear stress in the central region of the soil layer is low, indicating that the soil interface is often the main area of seepage failure.

The shear stress profile under different runoff depths is shown in Figure 6. The shear stress in the runoff region shows a linear growth trend with the increase in runoff water depth, and the shear stress on the water and soil interface gradually increases (Figure 6a), implying that the increase in runoff depth can intensify slope erosion. In addition, the increase in runoff depth has a slight effect on the shear stress distribution in the highly permeable soil layer (Figure 6b), while it has almost no

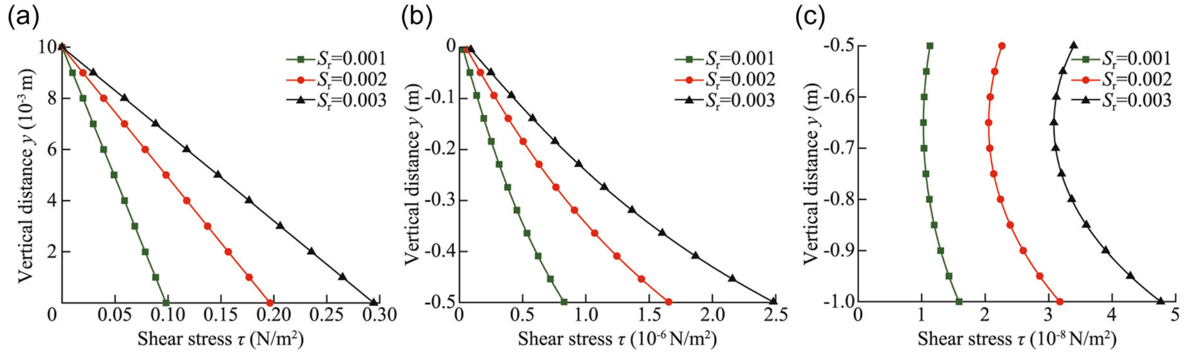

FIGURE 5 Shear stress profile under various slopes: (a) runoff flow; (b) seepage flow in the highly permeable soil layer; and (c) seepage flow in the weakly permeable soil layer.

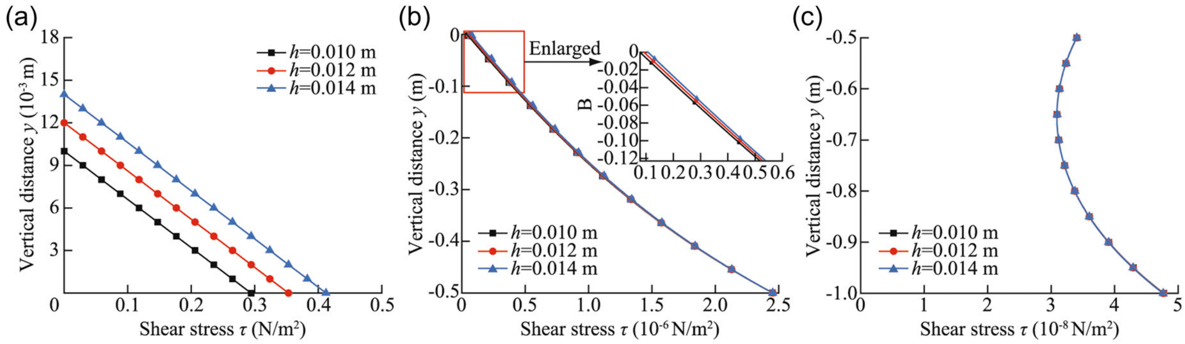

FIGURE 6 Shear stress profile under various runoff depths: (a) runoff flow; (b) seepage flow in the highly permeable soil layer; and (c) seepage flow in the weakly permeable soil layer.

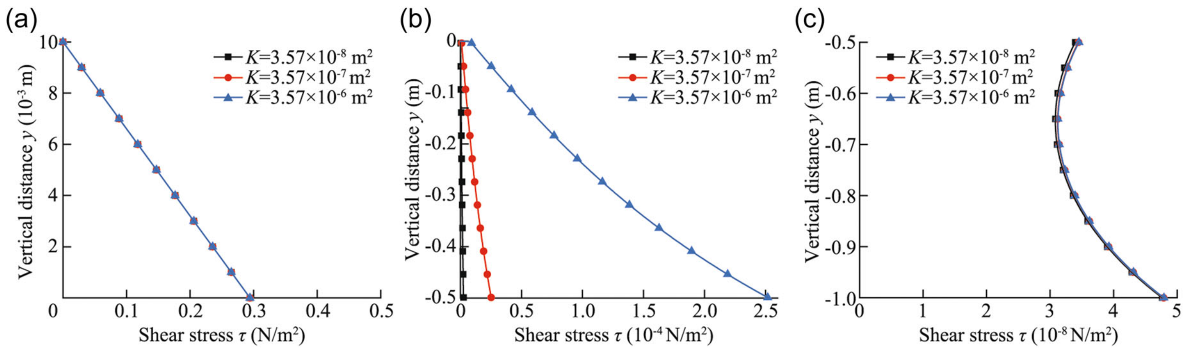

FIGURE 7 Shear stress profile under various permeabilities of the highly permeable soil layer: (a) runoff flow; (b) seepage flow in the highly permeable soil layer; and (c) seepage flow in the weakly permeable soil layer.

effect on the shear stress distribution in the weakly permeable soil layer (Figure 6c).

The shear stress profile in the runoff region does not change with increasing permeability of the highly permeable soil layer (Figure 7a). With the increase in permeability for the highly permeable soil layer, the shear stress within this region gradually increases, and the closer it is to the region bottom, the higher the shear stress value (Figure 7b). Furthermore, an increase in K_1 has a slight effect on the shear stress distribution at the top of the weakly permeable soil layer (Figure 7c).

3 | PARTICLE MOTION MODEL

From the previous analysis, it is known that the maximum shear stress appears at the water–soil interface, implying that the particle in this interface is most likely to be scoured. The force analysis of particles on the interface between soil and water is shown in Figure 8. Choi and Kwak (2001) noted that the incipient motion models of soil particles under the runoff effect mainly include the sliding model, the rolling model, and the lifting model. The nonuniform particles on the slope surface are assumed to

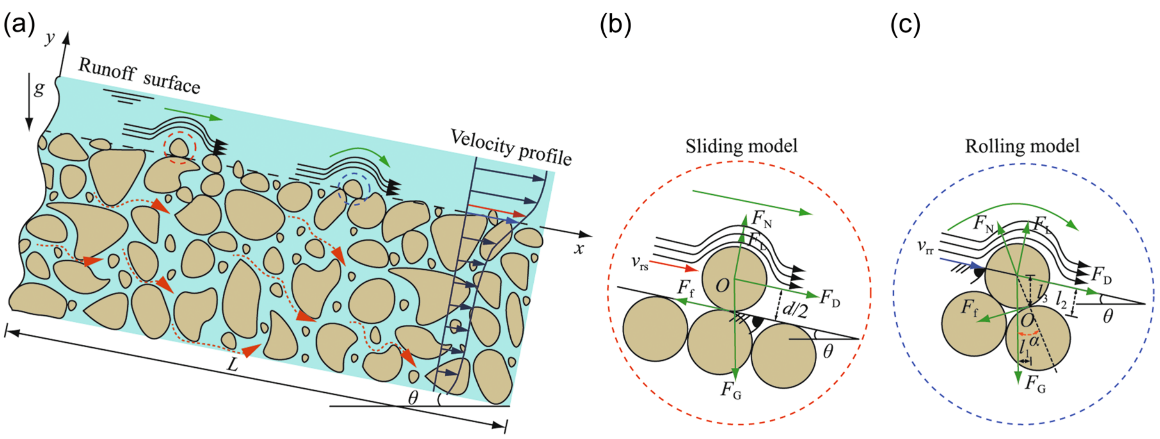

FIGURE 8 Particle incipient motion condition: (a) particle motion model; (b) force analysis of the sliding model; and (c) force analysis of the rolling model.

be standard spherical particles. There are mainly two types of particle instability at the interface, that is, the sliding model (Figure 8b) and the rolling model (Figure 8c).

The particles on the slope surface are mainly subjected to drag force F_D, lift force F_L, effective gravity F_G, support force F_N, and friction force F_f under the action of water flow, which are shown in Equations (51)–(55):

$$F_D = \frac{1}{8}\pi C_D \rho d_i^2 v_c^2, \tag{51}$$

$$F_L = \frac{1}{8}\pi C_L \rho d_i^2 v_c^2, \tag{52}$$

$$F_G = \frac{1}{6}\pi(\gamma_s - \gamma_w) d_i^3, \tag{53}$$

$$\begin{aligned} F_N &= F_G \cos\theta - F_L \\ &= \frac{1}{6}\pi(\gamma_s - \gamma_w) d_i^3 \cos\theta - \frac{1}{8}\pi C_L \rho d_i{}^2 v_c^2, \end{aligned} \tag{54}$$

$$\begin{aligned} F_f &= F_N \tan\varphi \\ &= \left[\frac{1}{6}\pi(\gamma_s - \gamma_w) d_i^3 \cos\theta - \frac{1}{8}\pi C_L \rho d_i^2 v_c^2\right] \tan\varphi, \end{aligned} \tag{55}$$

where C_D and C_L are the drag force coefficient and the lift force coefficient, respectively; $C_D = 0.4$ and $C_L = 0.2$ (Kirchner et al., 1990; Wiberg & Smith, 1985); d_i is the particle diameter; v_c is the flow velocity at the particle center; γ_s and γ_w are the unit weight of particle and the unit weight of water, respectively; and φ is the internal friction angle.

The force balance equation of a single particle can be expressed as follows when particle sliding instability occurs in Figure 8b:

$$F_D + F_G \sin\theta - F_f = 0. \tag{56}$$

By substituting Equations (51)–(55) into Equation (56), the critical velocity v_{cs} of particle motion under the sliding model can be calculated using Equation (57):

$$v_{cs} = \sqrt{\frac{4d_i(\gamma_s - \gamma_w)(\cos\theta \tan\varphi - \sin\theta)}{3\rho(C_D + C_L \tan\varphi)}}. \tag{57}$$

According to Equation (29), the runoff velocity expression v_{rc} at the sliding particle center on the slope surface ($y = d_i/2$) is shown in Equation (58):

$$v_{rs} = \left[-\frac{1}{8}(d_i/H)^2 + \frac{X_5}{2}(d_i/H) + X_6\right]\rho g \sin\theta H^2/\mu_f. \tag{58}$$

The particle will slide when $v_{rs} > v_{cs}$. Therefore, the particle sliding safety factor K_s can be defined as follows:

$$K_s = \frac{v_{cs}}{v_{rs}} = \frac{\sqrt{\frac{4d_i(G_s - 1)(\cos\theta \tan\varphi - \sin\theta)g}{3(C_D + C_L \tan\varphi)}}}{\left[-\frac{1}{8}(d_i/H)^2 + \frac{X_5}{2}(d_i/H) + X_6\right]\rho g \sin\theta H^2/\mu_f}, \tag{59}$$

where G_s is the particle-specific gravity.

The moment balance equation of a single particle at point O is as follows when particle rolling instability occurs in Figure 8c:

$$(F_G - F_L \cos\theta) l_1 - F_D l_2 - F_L \sin\theta l_3 = 0. \tag{60}$$

It can be inferred from geometric relations that $l_1 = d_i \sin\alpha/2$, $l_2 = \sqrt{3}\, d_i/4$, $l_3 = d_i \cos\alpha/2$, where α denotes the particle packing angle, which is in the range of 15°–40° (Mitchell & Soga, 2005).

Substituting Equations (51)–(55) into Equation (60), it can be concluded that

$$\begin{aligned} &\left[\frac{1}{6}\pi(\gamma_s - \gamma_w) d_i^3 - \frac{1}{8}\pi C_L \rho d_i^2 v_c^2 \cos\theta\right] d_i \sin\alpha/2 \\ &- \frac{1}{8}\pi C_D \rho d_i^2 v_c^2 \sqrt{3}\, d_i/4 - \frac{1}{8}\pi C_L \rho d_i^2 v_c^2 \sin\theta d_i \cos\alpha/2 = 0. \end{aligned} \tag{61}$$

The critical velocity v_{cr} of the particle incipient motion under the rolling model can be shown in Equation (62):

$$v_{\mathrm{cr}} = \sqrt{\frac{8g(G_{\mathrm{s}}-1)d_i \sin\alpha}{3[2C_{\mathrm{L}}\sin(\alpha+\theta)+\sqrt{3}C_{\mathrm{D}}]}}. \tag{62}$$

According to Equation (29), the runoff velocity expression v_{rr} at the rolling particle center on the slope surface ($y = 0$) is shown in Equation (63):

$$v_{\mathrm{rr}} = X_6 \rho g \sin\theta H^2/\mu_{\mathrm{f}}. \tag{63}$$

The particle will roll when $v_{\mathrm{rr}} > v_{\mathrm{cr}}$. Therefore, the particle rolling safety factor K_{r} can be defined as follows:

$$K_{\mathrm{r}} = \frac{v_{\mathrm{cr}}}{v_{\mathrm{rr}}} = \frac{\sqrt{\frac{8g(G_{\mathrm{s}}-1)d_i \sin\alpha}{3[2C_{\mathrm{L}}\sin(\alpha+\theta)+\sqrt{3}C_{\mathrm{D}}]}}}{X_6 \rho g \sin\theta H^2/\mu_{\mathrm{f}}}. \tag{64}$$

In fact, the particles on the slope surface are close to each other. The rolling motion is almost always for particle movement, while there are very few sliding motions. Therefore, slope particle scouring focuses on particle rolling. The slope particles are in a stable state, and erosion will not occur when $K_{\mathrm{r}} > 1$. The slope surface soil particles are in a critical state when $K_{\mathrm{r}} = 1$, while the slope surface particles will lose stability and rolling motion under the action of water flow.

4 | VALIDATION

To further validate the developed nonlinear mathematical models and mechanical equilibrium models, these models are compared with existing models by setting the properties of the two soil layers the same, as shown in Figure 9. Figure 9a compares the vertical velocity distribution of the models, where $n_1 = n_2 = 0.35$, $K_1 = K_2 = 6.12 \times 10^{-10}\ \mathrm{m}^2$, $b_1 = b_2 = 0.005\ \mathrm{m}$, $h = 0.015\ \mathrm{m}$, and $Sr = 0.0002$. The results of the current model are in good agreement with the semianalytical solution model of Hsieh and Yang (2013). Figure 9b compares the particle mobilization safety factor of the models, where the basic parameters are consistent with those of Liu et al. (2023). The safety factor calculated by the current model is identical to that of Ye et al. (2019), Yuan et al. (2019), and Liu et al. (2023) ($\beta = 0$, which is the stress jumping coefficient).

5 | ANALYSIS AND DISCUSSION

As shown in Equation (64), the particle rolling safety factor K_{r} is mainly affected by the slope macroscopic variables and particle mesoscopic parameters when the tunnel-slope surface particles undergo scouring. The tunnel-slope macroscopic parameters mainly include runoff depth h, slope angle θ, and soil permeability of the highly permeable region K_1. The particle mesoscopic parameters mainly include particle-specific gravity G_{s}, particle diameter d_i, and particle packing angle α. The sensitivity analysis is conducted for the above 6 parameters, whose ranges are listed in Table 1. Other parameters are as follows: $n_2 = 0.35$, $K_2 = 4.26 \times 10^{-10}\ \mathrm{m}^2$, and $b_1 = b_2 = 0.5\ \mathrm{m}$.

Under the action of water scouring, the influence of slope macroscopic parameters on the safety factor of particle rolling was studied and is shown in Figure 10. As the runoff depth increases, the rolling safety factor of particles gradually decreases, and the particles transition from a static state to a moving one (Figure 10a). The main reason for this is that increasing the water depth of runoff causes the shear stress of the slope surface to increase, and the particles are more prone to rolling instability. The rolling safety factor decreases with increasing slope angle (Figure 10b), indicating that steeper slopes are more prone to particle instability. Fu et al. (2011) and El Kateb et al. (2013) have also reported similar conclusions. Increasing the permeability of the highly permeable soil region decreases the rolling safety factor (Figure 10c), as the resistance of particles to water flow is negatively correlated with permeability. This leads to an increase in the fluid drag force on the surface particles, making particles more prone to instability. Therefore, increasing slope macroscopic parameters (runoff depth h, slope angle θ, and permeability K_1) can aggravate slope scoring erosion.

The influence of the particle mesoscopic parameters on the particle rolling safety factor is shown in Figure 11. The rolling safety factor of particles increases gradually

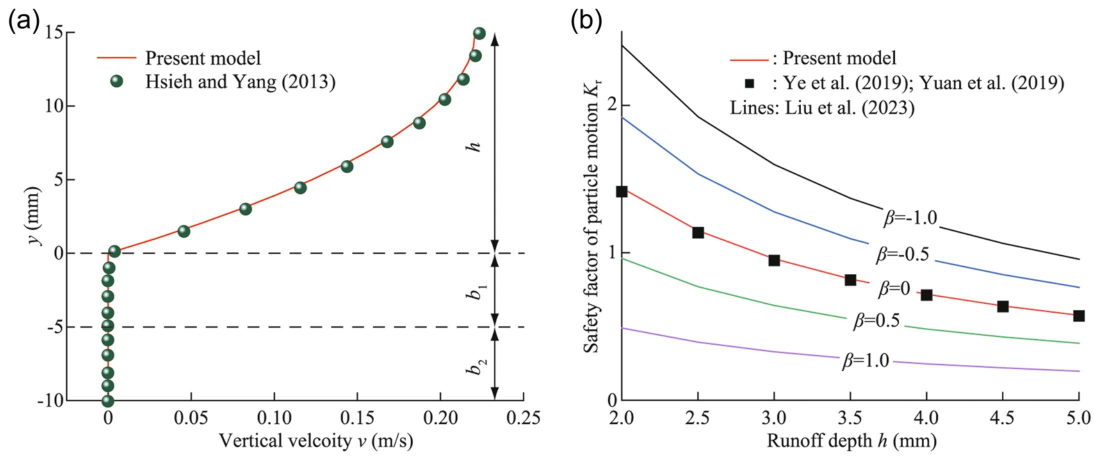

FIGURE 9 Model validation: (a) vertical velocity and (b) safety factor of particle motion.

TABLE 1 Reference values of the parameters.

Basic value range	Slope macroscopic parameters h (10^{-3} m)	θ (°)	K_1 (10^{-7} m^2)	Particle mesoscopic parameters d_i (10^{-3} m)	G_s	α (°)
Mean value	10	30	1.1	5	2.6	25
Parameter range	1–20	20–40	0.9–1.3	3–7	2.4–2.8	15–35

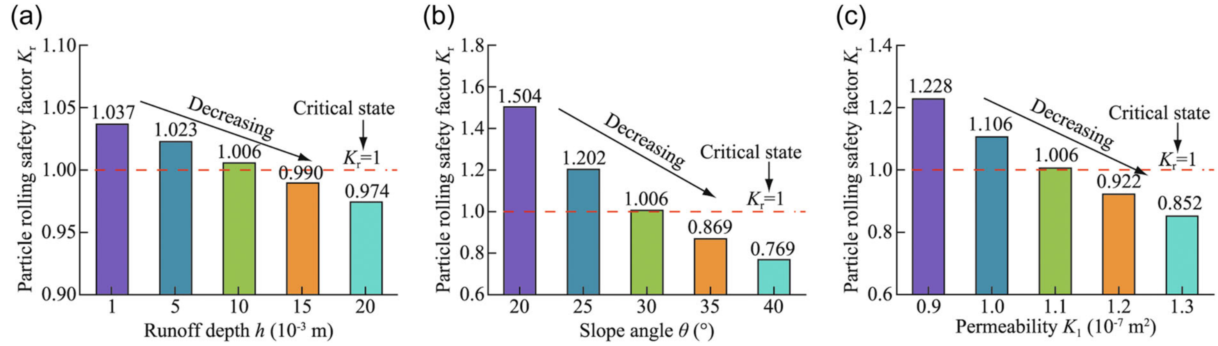

FIGURE 10 Influence of the slope macroscopic parameters on the particle state: (a) runoff depth h; (b) slope angle θ; and (c) permeability K_1.

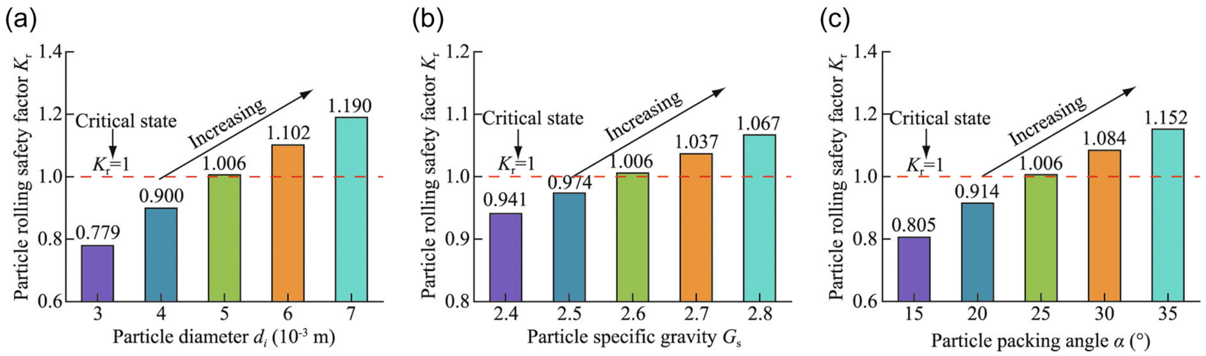

FIGURE 11 Influence of the particle mesoscopic parameters on the particle state: (a) particle diameter d_i; (b) particle-specific gravity G_s; and (c) particle packing angle α.

with increasing particle diameter on the slope surface (Figure 11a), implying that the smaller the surface particles, the more easily the particles are eroded. This conclusion was reported by Li et al. (2019). The greater the particle-specific gravity, the greater the rolling safety factor, and the stronger the scour resistance of the surface particles (Figure 11b). With increasing particle stacking angle, the rolling safety factor increases (Figure 11c). The main reason for this is that the larger the stacking angle of the particle, the greater the buried depth of the particle, and the greater the binding force of the surrounding particles on the target particle. Then, the anti-scouring ability of the target particle will thus be stronger. Therefore, increasing the particle mesoscopic parameters (particle diameter d_i, particle-specific gravity G_s, and particle packing angle α) is beneficial to soil and water conservation of slopes.

Limitations and future work:

1. The highly/weakly soil layers are assumed to be isotropic and homogeneous porous media. However, in reality, the soil layers of tunnel slopes may be anisotropic or heterogeneous, which could affect the fluid flow and particle motion in the soil layers. Future research could focus on investigation of the effects of anisotropic and heterogeneous soil layers on tunnel-slope erosion and development of a more realistic model that takes into account the anisotropy and heterogeneity of the soil layers.
2. The seepage flow is assumed to be saturated seepage. However, unsaturated seepage may also occur in tunnel slopes and could have a significant impact on the erosion process. Future research could focus on the study of the effects of unsaturated seepage on tunnel-slope erosion and development of a model that considers both saturated and unsaturated seepage.
3. The runoff and seepage are assumed to be steady laminar. However, in reality, the flow of water on tunnel slopes may be turbulent, which could affect the erosion process. Future research could focus on investigation of the effects of turbulent flow on tunnel-slope erosion and development of a model that considers both laminar and turbulent flow.

6 | CONCLUSIONS

1. A nonlinear mathematical model was proposed to investigate the velocity profile of the tunnel slope that contains three parts, that is, runoff region, highly permeable soil layer, and weakly permeable soil layer. In the model, the Navier–Stokes equation was used to govern runoff, while the Brinkman-extended Darcy equation was used to govern fast/slow seepage in the highly/weakly permeable soil layer.
2. The expressions of the velocity profile and shear stress were derived when the interface velocity and shear stress are continuous. The analysis reveals that the steeper the tunnel slope, the greater the velocity; the overall velocity in the runoff region gradually increases with increasing runoff depth, especially at the runoff free surface; increasing permeability in the highly permeable region only increases the velocity and stress in that region; and the maximum shear stress occurs at the water–soil interface, followed by the soil interface, and these interfaces are usually the key areas for erosion.
3. A single-particle mechanical equilibrium model was established to study the particle motion on the tunnel-slope surface under coupling between flow and particle. Safety factors of particle motion were derived based on the sliding model and the rolling model. Parameter sensitivity analysis shows that increasing runoff depth, slope angle, and permeability can intensify slope-scoring erosion, whereas increasing particle diameter, particle-specific gravity, and particle packing angle can enhance the erosion resistance of the slope surface.

ACKNOWLEDGMENTS

This study was funded by the National Natural Science Foundation of China (52109125), the Fundamental Research Funds for the Central Universities (2023ZYGXZRx2tjD2231010), and the Natural Science Foundation of Jiangsu Province (BK20231217).

CONFLICT OF INTEREST STATEMENT

The authors declare no conflict of interest.

DATA AVAILABILITY STATEMENT

The data that support the findings of this study are available from the corresponding author upon reasonable request. All data, models, or codes that support the findings of this study are available from the corresponding author upon reasonable request.

ORCID

Danqing Song http://orcid.org/0000-0003-1015-9544

REFERENCES

Agudo JR, Wierschem A. Incipient motion of a single particle on regular substrates in laminar shear flow. *Phys Fluids*. 2012;24(9): 20141. doi:10.1063/1.4753941

Akgun A, Turk N. Mapping erosion susceptibility by a multivariate statistical method: a case study from the Ayvalk region, NW Turkey. *Comput Geosci*. 2011;37(9):1515-1524. doi:10.1016/j.cageo.2010.09.006

Almalki WS, Hamdan MH. Investigations in effective viscosity of fluid in a porous medium. *Int J Eng Res Appl*. 2016;6(4):41-51.

Arnau-Rosalén E, Calvo-Cases A, Boix-Fayos C, Lavee H, Sarah P. Analysis of soil surface component patterns affecting runoff generation. An example of methods applied to Mediterranean hillslopes in Alicante (Spain). *Geomorphology*. 2008;101(4):595-606. doi:10.1016/j.geomorph.2008.03.001

Berger C, Schulze M, Rieke-Zapp D, Schlunegger F. Rill development and soil erosion: a laboratory study of slope and rainfall intensity. *Earth Surf Proces Landforms*. 2010;35(12):1456-1467. doi:10.1002/esp.1989

Chehlafi A, Kchikach A, Derradji A, Mequedade N. Highway cutting slopes with high rainfall erosion in Morocco: evaluation of soil losses and erosion control using concrete arches. *Eng Geol*. 2019; 260:105200. doi:10.1016/j.enggeo.2019.105200

Chen LL, Wang ZF, Wang YQ. Failure analysis and treatments of tunnel entrance collapse due to sustained rainfall: a case study. *Water*. 2022;14(16):2486. doi:10.3390/w14162486

Cheng NS, Wei M, Lu Y. Critical flow velocity for incipient sediment motion in open channel flow with rigid emergent vegetation. *J Eng Mech*. 2020;146(11):0001857. doi:10.1061/(ASCE)EM.1943-7889.0001857

Choi SU, Kwak S. Theoretical and probabilistic analyses of incipient motion of sediment particles. *KSCE J Civil Eng*. 2001;5(1):59-65.

Ciampalini R, Torri D. Detachment of soil particles by shallow flow: sampling methodology and observations. *Catena*. 1998;32(1):37-53. doi:10.1016/S0341-8162(97)00050-7

Cui Y, Jiang Y, Guo C. Investigation of the initiation of shallow failure in widely graded loose soil slopes considering interstitial flow and surface runoff. *Landslides*. 2019;16(4):815-828. doi:10.1007/s10346-018-01129-9

Dunkerley D. Percolation through leaf litter: what happens during rainfall events of varying intensity? *J Hydrol*. 2015;525:737-746. doi:10.1016/j.jhydrol.2015.04.039

Fox DM, Bryan RB. The relationship of soil loss by interrill erosion to slope gradient. *Catena*. 2000;38(3):211-222. doi:10.1016/S0341-8162(99)00072-7

Fu S, Liu B, Liu H, Xu L. The effect of slope on interrill erosion at short slopes. *Catena*. 2011;84(1-2):29-34. doi:10.1016/j.catena.2010.08.013

Guo T, Wang Q, Li D, Wu L. Sediment and solute transport on soil slope under simultaneous influence of rainfall impact and scouring flow. *Hydrol Process*. 2010;24(11):1446-1454. doi:10.1002/hyp.7605

Guo Z, Jeng DS, Zhao H, Guo W, Wang L. Effect of seepage flow on sediment incipient motion around a free spanning pipeline. *Coastal Eng*. 2019;143:50-62. doi:10.1016/j.coastaleng.2018.10.012

He L, Tafti D. Variation of drag, lift and torque in a suspension of ellipsoidal particles. *Powder Technol*. 2018;335:409-426. doi:10.1016/j.powtec.2018.05.031

Hsieh PC, Yang JS. A semi-analytical solution of surface flow and subsurface flow on a slope land under a uniform rainfall excess. *Int J Numer Anal Methods Geomech*. 2013;37(8):893-903. doi:10.1002/nag.1128

Jiao Q, Wang Y, Jiang W. The progressive failure mechanism of the tunnel-slope system under rainfall: an experimental investigation. *Geofluids*. 2022;2022:1-16. doi:10.1155/2022/1775049

El Kateb H, Zhang H, Zhang P, Mosandl R. Soil erosion and surface runoff on different vegetation covers and slope gradients: a field experiment in Southern Shaanxi Province, China. *Catena*. 2013; 105:1-10. doi:10.1016/j.catena.2012.12.012

Kim HS, Kimura I, Park M. Numerical simulation of flow and suspended sediment deposition within and around a circular patch of vegetation on a rigid bed. *Water Resources Res*. 2018;54(10): 7231-7251. doi:10.1029/2017WR021087

Kim HS, Nabi M, Kimura I, Shimizu Y. Computational modeling of flow and morphodynamics through rigid-emergent vegetation. *Adv Water Resources*. 2015;84:64-86. doi:10.1016/j.advwatres.2015.07.020

Kirchner JW, Dietrich WE, Iseya F, Ikeda H. The variability of critical shear stress, friction angle, and grain protrusion in water-worked sediments. *Sedimentology*. 1990;37(4):647-672. doi:10.1111/j.1365-3091.1990.tb00627.x

Li Y, Zhang F, Yang M, Zhang J, Xie Y. Impacts of biochar application rates and particle sizes on runoff and soil loss in small cultivated loess plots under simulated rainfall. *Sci Total Environ*. 2019;649:1403-1413. doi:10.1016/j.scitotenv.2018.08.415

Lin J, Krom MD, Wang F, Cheng P, Yu Q, Chen N. Simultaneous observations revealed the nonsteady state effects of a tropical storm on the export of particles and inorganic nitrogen through a river-estuary continuum. *J Hydrol*. 2022;606:127438. doi:10.1016/j.jhydrol.2022.127438

Liu J, Chen Z, Kanungo DP, et al. Topsoil reinforcement of sandy slope for preventing erosion using water-based polyurethane soil stabilizer. *Eng Geol*. 2019;252:125-135. doi:10.1016/j.enggeo.2019.03.003

Liu Q, Xu X, Lin L, Wang D. Occurrence, distribution and ecological risk assessment of polycyclic aromatic hydrocarbons and their derivatives in the effluents of wastewater treatment plants. *Sci Total Environ*. 2021;789:147911. doi:10.1016/j.scitotenv.2021.147911

Liu QQ, Xiang H, Singh VP. A simulation model for unified interrill erosion and rill erosion on hillslopes. *Hydrol Process*. 2006;20(3):469-486. doi:10.1002/hyp.5915

Liu XX, Chiew YM. Effect of seepage on initiation of cohesionless sediment transport. *Acta Geophys*. 2012;60(6):1778-1796. doi:10.2478/s11600-012-0043-7

Liu Y, Zhang S, Fu W, Song D, Wang C, Ye F. Incipient motion criteria of wide-grading particles on loose soil slopes under coupling of runoff and seepage. *Int J Geomech*. 2023;23(5):8091. doi:10.1061/IJGNAI.GMENG-8091

Ma JQ, Fu HY, Wang GY, Zeng L, Shi ZL. Seepage characteristics of layered soil slope under rainfall conditions. *J Central South Univ (Sci Technol)*. 2018;49(2):464-471. doi:10.11817/j.issn.1672-7207.2018.02.027

Mendes P, Maier I, Thomsen L. Effect of physical variables on particle critical erosion shear stress: hydrostatic pressure, slope and changes in water density. *Estuarine Coast Shelf Sci*. 2007;75(3):317-326. doi:10.1016/j.ecss.2007.04.035

Mitchell JK, Soga K. *Fundamentals of Soil Behavior*. Wiley; 2005.

Patricia L, Wiberg J, Dungan S. Calculations of the critical shear stress for motion of uniform and heterogeneous sediments. *Water Resources Res*. 1987;23(8):1471-1480. doi:10.1029/WR023i008p01471

Piqué G, Vericat D, Sabater S, Batalla RJ. Effects of biofilm on riverbed scour. *Sci Total Environ*. 2016;572:1033-1046. doi:10.1016/j.scitotenv.2016.08.009

Rabinovich E, Kalman H. Incipient motion of individual particles in horizontal particle–fluid systems: B. theoretical analysis. *Powder Technol*. 2009;192(3):326-338. doi:10.1016/j.powtec.2009.01.014

Shen H, He Y, Hu W, et al. The temporal evolution of soil erosion for corn and fallow hillslopes in the typical mollisol region of northeast China. *Soil Tillage Res*. 2019;186(3-4):200-205. doi:10.1016/j.still.2018.10.024

Sugioka KI, Komori S. Drag and lift forces acting on a spherical water droplet in homogeneous linear shear air flow. *J Fluid Mech*. 2007;570:155-175. doi:10.1017/S0022112006003065

Tsai HS, Wang Y, Liu C, Wang T, Huo M. The elemental 2D materials beyond graphene potentially used as hazardous gas sensors for environmental protection. *J Hazard Mater*. 2022;423:127148. doi:10.1016/j.jhazmat.2021.127148

Wang L, Guo F, Wang S. Prediction model of the collapse of bank slope under the erosion effect of wind-induced wave in the three gorges reservoir area, China. *Environ Earth Sci*. 2020;79:421. doi:10.1007/s12665-020-09169-y

Wei H, Wu D, Wu H, Tang L, Wang S, Sun H. Coordinated evolution and mechanism characteristics of the tunnel–landslide system under rainfall conditions. *Eng Failure Anal*. 2023;146:107118. doi:10.1016/j.engfailanal.2023.107118

Wei Y, Xia M, Ye F, Fu W. Effect of drag force on stability of residual soil slopes under surface runoff. *Geomat Nat Hazards Risk*. 2018;9(1):488-500. doi:10.1080/19475705.2018.1447518

Wiberg PL, Smith JD. A theoretical model for saltating grains in water. *J Geophys Res: Oceans*. 1985;90(C4):7341-7354. doi:10.1029/JC090iC04p07341

Xie L, Lei H, Yu Y, Sun X. Incipient motion of riverbank sediments with outflow seepage. *J Hydraulic Eng*. 2009;135(3):228-233. doi:10.1061/(ASCE)0733-9429(2009)135:3(228)

Xiong W, Tang P, Kong B, Cai CS. Computational simulation of live-bed bridge scour considering suspended sediment loads. *J Comput Civil Eng*. 2017;31(5):04017040. doi:10.1061/(ASCE)CP.1943-5487.0000689

Ye F, Fu W, Yuan X, Xiang Y. Drag force effect of surface runoff on stability of shallow soil slope. *Soil Mech Found Eng*. 2019;56(1):12-20. doi:10.1007/s11204-019-09563-0

Yergey BA, Beninati ML, Marshall JS. Sensitivity of incipient particle motion to fluid flow penetration depth within a packed bed. *Sedimentology*. 2010;57(2):418-428. doi:10.1111/j.1365-3091.2009.01088.x

Yuan X, Zheng N, Ye F, Fu W. Critical runoff depth estimation for incipient motion of noncohesive sediment on loose soil slope under heavy rainfall. *Geomat, Nat Hazards Risk*. 2019;10(1):2330-2345. doi:10.1080/19475705.2019.1697760

Zastawny M, Mallouppas G, Zhao F, van Wachem B. Derivation of drag and lift force and torque coefficients for nonspherical particles in flows. *Int J Multiphase Flow*. 2012;39(1):227-239. doi:10.1016/j.ijmultiphaseflow.2011.09.004

Zhai HL, Jeng DS, Guo Z, Liang ZD. Impact of two-dimensional seepage flow on sediment incipient motion under waves. *Appl Ocean Res*. 2020;108:102510. doi:10.1016/j.apor.2020.102510

Zhan TLT, Jia GW, Chen YM, Fredlund DG, Li H. An analytical solution for rainfall infiltration into an unsaturated infinite slope and its application to slope stability analysis. *Int J Numer Anal Methods Geomech*. 2013;37(12):1737-1760. doi:10.1002/nag.2106

Zhang S, Liu X. Theoretical, experimental, and numerical studies of flow field characteristics and incipient scouring erosion for slope with rigid vegetations. *J Hydroly* 2023;622:129638. doi:10.1016/j.jhydrol.2023.129638

Zhang S, Ye F, Fu WX. Permeability characteristics of porous rock with conduits under Stokes-Brinkman-Darcy coupling model. *Int J Geomech*. 2021;21(6). doi:10.1061/(ASCE)GM.1943-5622.0002026

Zhang S, Zhang B, Ye F, Fu WX. A closed-form solution for free- and seepage-flow field in axisymmetric infilled conduit. *Groundwater*. 2021;60(1):112-124. doi:10.1111/gwat.13126

Zhao E, Qu K, Mu L. Numerical study of morphological response of the sandy bed after tsunami-like wave overtopping an impermeable seawall. *Ocean Engineering*. 2019;186:1-23. doi:10.1016/j.oceaneng.2019.05.058

AUTHOR BIOGRAPHY

Danqing Song, graduated from Shanghai Jiao Tong University in September 2019 (advisor: Academician Ge Xiurun) and worked as a postdoctoral researcher in the Department of Hydraulic Engineering at Tsinghua University from November 2019 to April 2023 (collaborative advisor: Academician Zhang Jianmin). He previously served as an assistant to the dean of the China Ocean Engineering Research Institute. He has long been engaged in research on rock mechanics related to slope and tunnel engineering geology and has participated in the evaluation and control of the deformation and stability of high slopes and deep-buried tunnels in major projects such as the Sichuan-Tibet Railway. He has presided over 10 national/provincial-level projects, including one National Natural Science Foundation project, two sub-projects of the National Key R&D Program, one subproject of the National Natural Science Foundation Major Project, and so forth. He has published more than 60 SCI papers, applied for 22 invention patents (seven authorized), and participated in the drafting of three industry/group standards as the second/main drafter. He has won eight scientific and technological awards, including the second prize of the Henan Province Science and Technology Progress Award (two as the first completion person and five as the second completion person), and was selected for the “New Century Excellent Talents Support Program” of the Ministry of Human Resources and Social Security and the “Water and Wood Scholars” program of Tsinghua University. He serves as a young editorial board member/editor for several international journals, including IJMST (a top-tier journal in the first district of the Chinese Academy of Sciences).

How to cite this article: Zhang S, Song D, Zhang R, Zhang K, Zhao Q, Sharma S. Flow field analysis and particle erosion of tunnel-slope systems under coupling between runoff and fast (slow) seepage. *Deep Undergr Sci Eng*. 2024;3(4):385-398. doi:10.1002/dug2.12062